Mechatronics 78 (2021) 102605

Contents lists available at ScienceDirect

Mechatronics

journal homepage: www.elsevier.com/locate/mechatronics

Design and validation of cable-driven hyper-redundant manipulator with a closed-loop puller-follower controller

Yang Zheng [a], Baibo Wu [a], Yuyang Chen [b], Lingyun Zeng [a], Guoying Gu [a], Xiangyang Zhu [a], Kai Xu [a,*]

[a] School of Mechanical Engineering, Shanghai Jiao Tong University, Shanghai, 200240, China
[b] UM-SJTU Joint Institute, Shanghai Jiao Tong University, Shanghai, 200240, China

ARTICLE INFO

Keywords:
Cable actuation
Closed-loop control
Hyper-redundant manipulator
Magnetic angle sensor
Puller-follower controller

ABSTRACT

A slim manipulator with redundant degrees of freedom can be of great use for inspection and maintenance in confined spaces. Cable-actuation is often preferred because of the possible proximal placement of the actuators. However, tension induced elongation and friction of the cables may substantially vary under different manipulator poses. It is then difficult to achieve high positioning accuracy under different loading conditions, even when such a manipulator went through careful motion calibration and actuation compensation. This paper hence proposes a 12-section cable-driven hyper-redundant manipulator with 24 degrees of freedom and closed-loop control. Customized magnetic angle sensors were integrated at each joint with a carefully designed sensor communication network to achieve rapid joint feedback. A novel puller-follower controller was proposed to properly actuate three cables for each universal joint that connects adjacent manipulator sections. The two joint angles of the universal joint and the cable tensions can be simultaneously controlled with the proposed puller-follower controller. The design overview, system descriptions, kinematics and experimental characterizations are reported in detail. After automatic straightening from arbitrary initial statuses, the proposed manipulator can achieve $\pm 0.5^{\circ}$ precision at each joint, even under a tip load up to 500 g.

1. Introduction

Redundant manipulators with slim bodies and high dexterity are capable of completing demanding tasks in confined space, such as the inspection, cleaning and maintenance in aerospace [1], nuclear [2], and medical industries [3]. With more motion DoFs,[1] hyper-redundant manipulators have several advantages, such as obstacle avoidance [4] and follow-the-tip motions [5].

Since the development of the hyper-redundant tensor arm manipulator [6] in the 1960s, quantities of hyper-redundant manipulators have been proposed. They can be classified by their structures as follows.

1) Articulated multi-section structures: the manipulator usually consists of serially articulated rigid links, implemented with either integrated actuators [7–11], or proximally arranged actuators [12–17].

2) Continuum mechanisms: the manipulator is composed of stacked continuum segments whose motion is realized by the deformation of the composed material. The continuum mechanism brings advantages such as compliance for safe interaction with the environment, compact structural designs, and dexterity in confined spaces [18]. It seems promising for field manipulation [19], industrial inspection [20], or minimally invasive surgery [21]. However, the relatively low stiffness and motion precision of the continuum mechanism are the major limitations.

Cables (or tendons) have been extensively employed in hyper-redundant manipulators, due to their capability to enable lightweight structural designs, scalable sizes, and environmental compatibility (e.g., applications underwater or with electromagnetic noises), etc. However, such benefits come with the requirements of properly maintaining the cables tensions: the tensions are necessary to provide outputs and can improve the joint stiffness, but high cable tension brings noticeable friction and cable elongation (i.e. the axial elastic deformation of the cable).

This paper was recommended for publication by Associate Editor Cong Wang.
* Corresponding author at: School of Mechanical Engineering, Shanghai Jiao Tong University, RM 916, ME BLDG, Shanghai, 200240, China.
E-mail address: k.xu@sjtu.edu.cn (K. Xu).
[1] DoF: Degree of Freedom.

https://doi.org/10.1016/j.mechatronics.2021.102605
Received 20 January 2021; Received in revised form 5 May 2021; Accepted 19 June 2021
Available online 5 July 2021

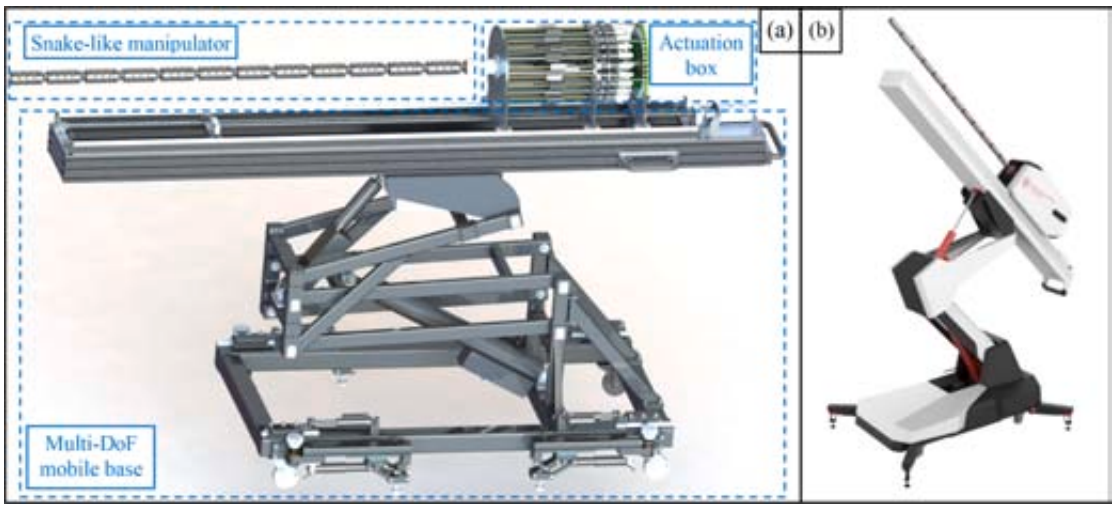

Fig. 1. Overview of the CDHM system: (a) configuration of the CDHM system; (b) overall appearance.

Among the investigations on existing cable-driven CDHMs,[2] the focus is placed onto the kinematics-based open-loop control [14,17]], the dynamics-based open-loop control [15], motion planning [22], etc. However, tension induced elongation and friction along the cables may substantially vary under different manipulator poses. It is then difficult to achieve high positioning accuracy under different loading conditions, even when such a manipulator went through careful motion calibration and actuation compensation. This paper hence proposes a 12-section CDHM with 24 DoFs and the corresponding closed-loop controller. It should be noted that it is not trivial to collect joint angle feedback to form a closed-loop controller, besides the necessity of carefully designing sensor communication network to achieve rapid joint angle readings. According to the preliminary results reported in the conference paper [23], the cables underwent gradual slack if only the joint angles are under closed-loop control. Even though a few approaches of measuring the joint angles were proposed in [24,25] (e.g., via an optical fiber or via distance measurements of adjacent joint structures), no existing approaches can be directly adopted for the closed-loop control. In the existing approaches, either the cable actuation lengths are calculated according to the kinematics models [14,17], or the cable actuation tensions are calculated according to the dynamics models [15].

In order to simultaneously realize the closed-loop control of the joint angles while maintaining the cable tensions by controlling the cable elongations, a puller-follower concept was introduced, for the first time, to design the proposed closed-loop controller for this new scenario where three cables antagonistically actuate a universal joint. In the work, the cable tension control was realized by regulating the cable elongation. Thus, the actuating motors all work in the position-servo mode and the force control loop is not required. Previously, the puller-follower controller was only applied in 1-DoF antagonistic cable actuation [26–28]. The proposed three-cable puller-follower controller may seem similar to the closed-loop controller in [29]. But the key difference is that the controller in [29] is only based on the cable-joint kinematics and no tension control was considered. Furthermore, a prediction-based feedforward compensator was incorporated to reduce the delay of the response mainly caused by the role switching between the puller cable and the follower cable.

Based on the previously proposed CDHM prototype [23], this paper presents a CDHM system that is mainly composed of a rigid-linked snake-like manipulator with 12 sections and 12 universal joints, as shown in Fig. 1. Substantially more works have been included in the present investigation, including: i) a multi-DoF mobile base has been added for various operational scenarios, as shown in Fig. 1; ii) the CDHM's joint sensors were carefully re-designed, where magnetic sensors were utilized to provide smooth and accurate joint feedback; iii) the closed-loop puller-follower controller was modified to handle the multi-section control while simultaneously maintaining cable tensions; and iv) prediction-based feedforward compensator is incorporated to reduce the delay mainly caused by the role switching between the puller cable and the follower cable.

This paper is organized as follows. First, the design goals and system overview are reported in Section 2. Then the CDHM system description is elaborated in Section 3, including the mechanical designs and the control infrastructure implementation. In Section 4, the kinematics model and the closed-loop puller-follower controller of the CDHM system is developed. The experimental characterizations and results are reported in Section 5. At last, the conclusion is summarized in Section 6.

2. Design goals and overview

As shown in Fig. 1(a), the CDHM system consists of a snake-like manipulator with 12 articulated sections. Each section has a 2-DoF cable-driven universal joint. The system hence possesses 24 DoFs to provide sufficient reachability and distal dexterity in confined spaces. Due to the manipulator's long reach and cantilever-like load condition under gravity, both motion accuracy and payload capability are substantially affected by the tension-induced cable elongation. To address these challenges, on-board angle sensors were utilized to realize joint angle feedback for closed-loop control, which can substantially reduce the positioning errors caused by cable elongation. With the closed-loop controller, the CDHM system also promises the motion accuracy under external load, leading to an enhanced payload capability.

Drawing on the aforementioned concepts, several key design goals are proposed as follows.

1) To provide sufficient dexterity for intra-cavity operation, the total length of the CDHM shall be over 1.5 m, and the universal joints should have a motion range no less than 45°.
2) The rotary errors for the joint angles shall be controlled within ±0.5° (a. k. a., a 0.5° control dead zone). Setting higher joint control goal may result in longer time to reach a steady status.
3) The tensions on the actuation cables shall be maintained within an acceptable range to avoid fracture and slackness (shown as an axial elongation below 2 mm).
4) The payload capability of the CDHM shall be at least 500 g (about one third of the snake-like manipulator's weight) which allows

[2] CDHM: Cable-Driven Hyper-redundant Manipulator.

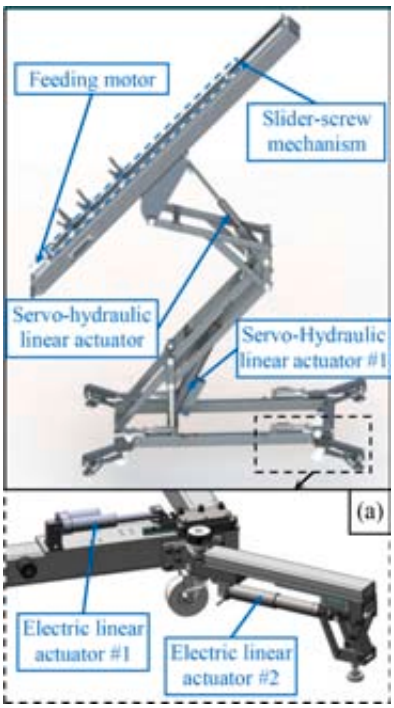

Fig. 2. Design of the multi-DoF mobile base: (a) the unfoldable supporting leg.

setting external end-effectors such as water jet for cleaning and soft grippers for maintenance operations.

3. System descriptions

Based on the abovementioned design goals, the CDHM system was designed and constructed. The system can be divided into three main components: the snake-like manipulator, the actuation box and the multi-DoF mobile base. This section presents the mechanical designs and control infrastructure of the CDHM system in detail.

3.1. Multi-DoF mobile base

To facilitate the operation of the CDHM system for various possible working scenarios, the multi-DoF mobile base was designed with several DoFs. The completely expanded state is shown in Fig. 2. The main features are described as follows.

1) The base can be conveniently moved with the four caster wheels. To acquire a stable working state, 4 unfoldable supporting legs were designed as shown in Fig. 2(a). The electric linear actuator #1 can provides the angular unfolding motion while the electric linear actuator #2 can support the whole system for a stable working state.
2) The base height of the snake-like manipulator can be adjusted with the servo-hydraulic linear actuator #1, whereas the servo-hydraulic linear actuator #2 can help adjust the pitch angle from 0° to 45°
3) To accomplish intra-cavity tasks, a feeding DoF is provided via a motorized slider-screw mechanism a feeding motor.

3.2. Snake-like manipulator and the actuation box

The snake-like manipulator consists of 12 rigid arm tubes connected by universal joints. Each arm tube and a proximally attached universal joint is addressed as a section, as demonstrated in Fig. 3(a).

The universal joint contains two orthogonally arranged revolute joints that connect a base support, a connecting hollow block, and an end support, as shown in Fig. 3(b). The cables that actuate the universal joints are attached to the end support and can slide in the holes in the base support. Two of the connecting shafts in the universal joint are hollow to accommodate the magnetic disks, which generate variable magnetic fields as the joint rotates, as shown in Fig. 3(c). All the structural components were made of aviation aluminum alloy (7076-T6), while the cables were ϕ1-mm stainless steel ropes with 200-N allowable tension. A digital camera module (Sony IMX 322) with 1920 × 1080 resolution was integrated in the distal end of the snake-like manipulator for visual inspection.

Two contactless magnetic rotary potentiometers (AS5600 from Advanced Monolithic Systems) are integrated on two neighborly placed sensor boards in each universal joint to provide angle feedback, as shown in Fig. 3(d). They replaced the resistor-based potentiometers in the joints that were reported in the authors' previous work [23], for improved feedback accuracy. When the joint angles of the universal joint change, the sensor can detect the variation of the magnetic field produced by the embedded magnet disks. The sensor provides absolute angle information with 360° measurement range and 12-bit resolution, which indicates a 0.088° angular sensitivity. Within each universal joint, two magnetic disks are neighborly placed. To eliminate the magnetic interference from the other nearby magnetic disk, customized shielding cases made by silicon steel sheets were used to cover the AS5600 magnetic rotary potentiometers. For every four magnetic sensors, a customized acquisition board was designed with an integrated CAN transceiver (SN65HVD1050DR, TI Inc.) and an F103 microcontroller (STMicroelectronics Inc.), as shown in Fig. 3(e). The F103 acquisition board is connected with the AS5600 sensor boards via IIC (Inter-Integrated Circuit) communication protocol.

The actuation box is proximal to the 1st section of the snake-like manipulator. The actuation box consists of 36 actuation units, each of which further includes a brushless servo motor (ECX22 from Maxon) and a slider-screw assembly. The 36 actuation units are compactly arranged in two layers: 24 units in the outer layer and 12 units in the inner layer, as shown in Fig. 4. Other devices such as the control boards, network switch, industrial PC, etc., were also integrated in the actuation box. A teaching panel with a touch screen and a joystick was integrated for teleoperation and system control. The overall size of the actuation box is ϕ324 mm × 590 mm, and its total mass is around 53 kg. The structural parameters of the constructed CDHM system are listed in Table I, which satisfy the design goals presented in Section 2.

3.3. Control infrastructure and software

The architecture of the CDHM system's control infrastructure can be divided into two levels, as shown in Fig. 5.

The upper level includes an industrial PC, the touch screen, and the digital camera. The industrial PC, with a 2.4 GHz CPU and a 4 GB RAM, runs programs for motion planning, kinematics, closed-loop control, as well as the graphic user interface displayed on the touch screen. The programs were developed in Linux. The digital camera was connected to the industrial PC via a USB cable.

The lower level includes six F407 microcontrollers and other connected control electronics. The F407 microcontrollers all communicate with the industrial PC via UDP protocol over a LAN. The first F407 is used for the data acquisition of the control inputs from the operating joystick. There are 36 Maxon servo motors to be controlled and 24 joint sensors to be read for the 12 universal joints. As shown in Fig. 5, every two F103 acquisition boards are connected with one F407 microcontroller and each F103 acquisition boards collects readings from four sensors. Hence, three F407 microcontrollers collect the readings from the 24 joint sensors. Each F407 microcontroller is used to send control signals to 9 EPOS 36/2 controllers via CAN bus. Hence, four F407 microcontrollers are used to control the 36 Maxon servo motors. The sixth F407 microcontroller is used to control the Yaskawa AC motor for the feeding motion as well as the servo-hydraulic actuators and the electric actuators in the mobile base via the controller's I/O interface.

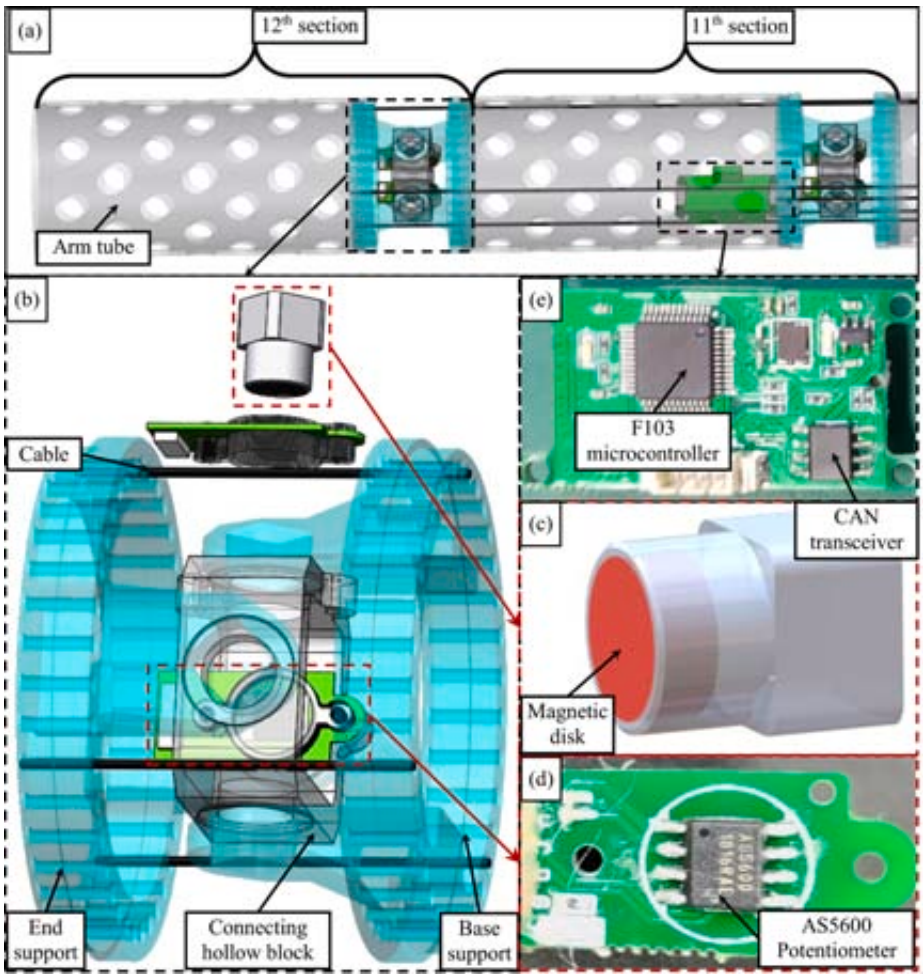

Fig. 3. Design of the snake arm: (a) the distal two sections; (b) structure of a universal joint; (c) the hollow connecting shaft with a magnet disk; (d) the AS5600 sensor board; and (e) the F103 acquisition board.

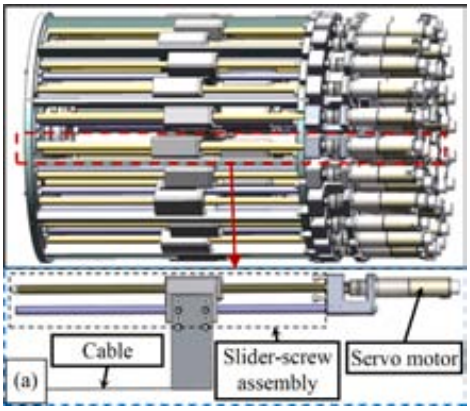

Fig. 4. Actuation box: (a) an actuation unit.

4. Kinematics and closed-loop controller

In this section, the actuation kinematics model is first presented in Section 4.1. To eliminate joint angle errors caused by cable elongation while maintaining cable tensions for slackness avoidance, a puller-follower closed-loop controller is then designed, as detailed in Section 4.2. The manipulator kinematics is introduced in Section 4.3.

Several coordinates are first defined to facilitate the derivations of the kinematics model, as referred to Fig. 6. The nomenclatures used in the kinematics model and the control framework are presented in Table II.

Table I
Structural parameters of the CDHM system.

Description	Quantity
Diameter of snake-like manipulator	55 mm
Section length (including the corresponding universal joint)	150 mm
Total length of the snake-like manipulator	1800 mm
Maximum joint angles of the universal joints	45°
Height variation range of the mobile base	900 mm
Pitch angle motion range of mobile base	45°

- Universal joint coordinate: $\{ui\} = \{\hat{x}_{ui}, \hat{y}_{ui}, \hat{z}_{ui}\}$ is attached to the center of the universal joint of the i^{th} section. $\hat{x}_{ui}$ and $\hat{y}_{ui}$ coincide with the axes of two revolute joints (designated in red and green dashed lines in Fig. 6.
- Base support coordinate: $\{bi\} = \{\hat{x}_{bi}, \hat{y}_{bi}, \hat{z}_{bi}\}$ is attached to the front surface of the base support of the i^{th} section. $\hat{z}_{bi}$ coincides with the central axis of the ith base support, whereas $\hat{x}_{bi}$ is parallel to $\hat{x}_{ui}$.
- End support coordinate: $\{ei\} = \{\hat{x}_{ei}, \hat{y}_{ei}, \hat{z}_{ei}\}$ is attached to the front surface of the end support disk of the i^{th} section. $\hat{z}_{ei}$ coincides with the central axis of the ith arm tube, whereas $\hat{y}_{ei}$ is parallel to $\hat{y}_{ui}$.
- Manipulator base coordinate: $\{w\} = \{\hat{x}_w, \hat{y}_w, \hat{z}_w\}$ is a stationary global reference coordinate. $\{b1\}$ is obtained from $\{w\}$ by a translation along $\hat{z}_w$.

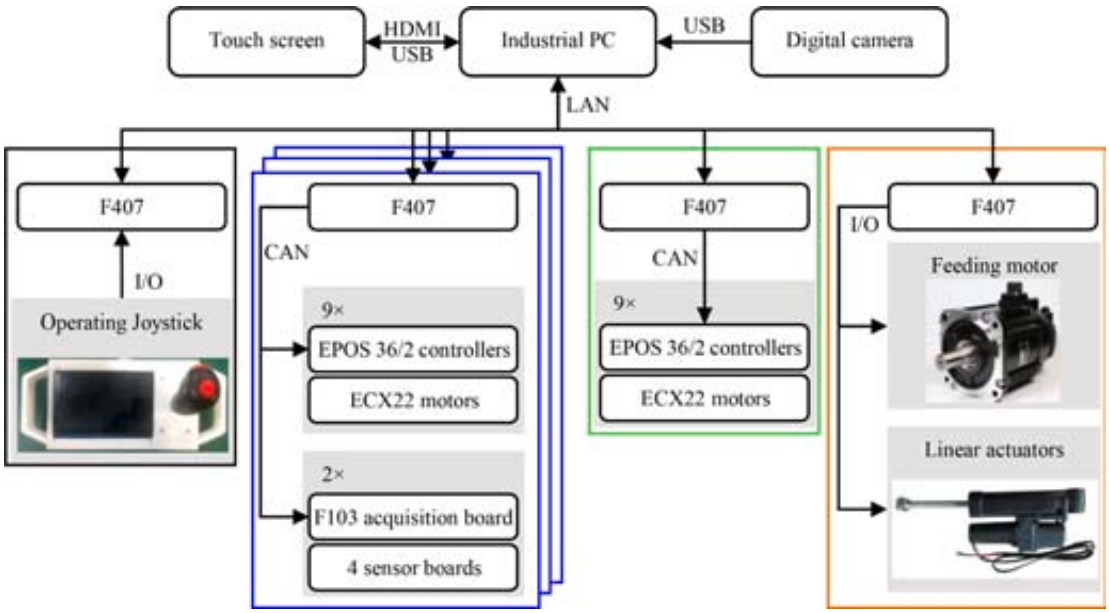

Fig. 5. Control infrastructure diagram.

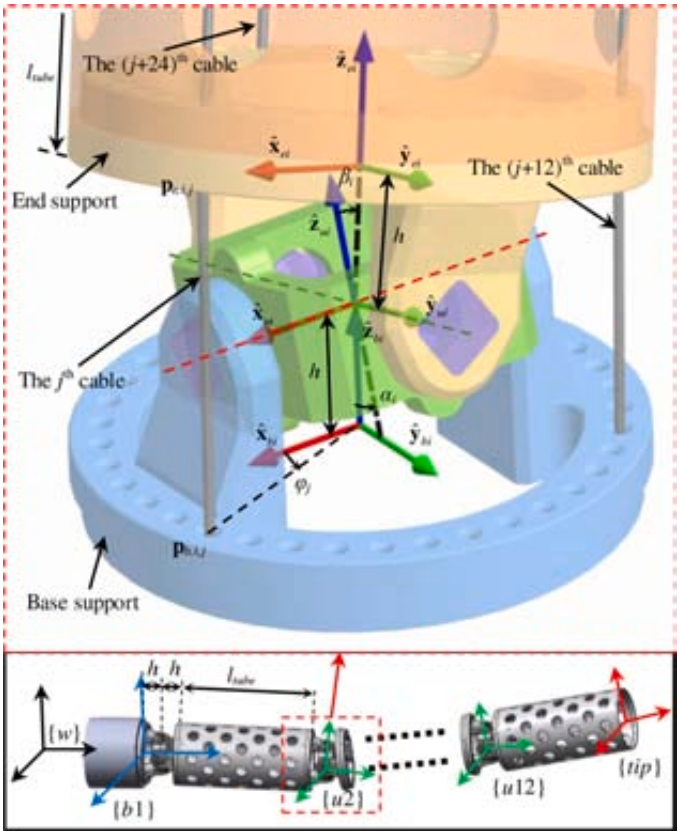

Fig. 6. Definition of the coordinates and kinematic variables.

- Manipulator tip coordinate: $\{tip\} = \{\hat{x}_{tip}, \hat{y}_{tip}, \hat{z}_{tip}\}$ is attached to the tip of the 12th arm tube. $\{tip\}$ is obtained from $\{e12\}$ by a translation along $\hat{z}_{e12}$ by l_{tube}.

4.1. Actuation kinematics

Firstly, $\mathbf{p}_{b,i,j}$ and $\mathbf{p}_{e,i,j}$, the intersection points of the xy-plane of coordinates $\{bi\}$ (or $\{ei\}$) with the j^{th} cable, can be expressed in a homogeneous form in $\{bi\}$ and $\{ei\}$ respectively:

$$^{bi}\mathrm{P}_{b,i,j} = {}^{bi}\mathrm{P}_{e,i,j} = \begin{bmatrix} r\cos\phi_j & r\sin\phi_j & 0 & 1 \end{bmatrix}^T \tag{1}$$

The homogeneous transformation from $\{bi\}$ to $\{ei\}$ is

$$^{bi}\mathbf{T}_{ei} = {}^{bi}\mathbf{T}_{ui}{}^{ui}\mathbf{T}_{ei}, \tag{2}$$

Where

Table II
Nomenclatures used in the kinematics model and the controller.

Symbol	Definition
i	Index of the sections, denoted from the proximal end to the distal end. i = 1, 2, …, 12.
j	Index of the cables. j = 1, 2, …, 36.
φ_j	The angle from $\hat{x}_{bi}$ to the line pointing from the center of {bi} to $\mathbf{p}_{b,i,j}$ about $\hat{z}_{bi}$, indicating the circumferential location of the j^{th} cable. $\varphi_j = (j-1)\pi/18$.
n_j	Index of the section where the j^{th} cable is the driving cable.
$l_{i,j}$	Distance between points $\mathbf{p}_{b,i,j}$ and $\mathbf{p}_{e,i,j}$. $l_{i,j}$ represents the length of the j^{th} cable in the i^{th} universal joint.
q_j	Actuation length of the j^{th} cable calculated from the actuation kinematics.
q_{ja}	Actuation length of the j^{th} cable calculated from the cable-driving motor encoder reading.
α_i, β_i	α_i is the rotation angle from $\hat{z}_{bi}$ to $\hat{z}_{ui}$ about $\hat{x}_{bi}$, whereas β_i is the rotation angle from $\hat{z}_{ui}$ to $\hat{z}_{ei}$ about $\hat{x}_{ui}$.
h	Distance between the origins of coordinates {bi} (or {ei}) and coordinates {ui}.
r	Distribution radius of the cable holes in the base or end supports.
l_{tube}	Length of the arm tube.
ε_j	Elongation of the j^{th} cable, relative to the initial status after initial tension. A negative ε_j represents an increased elongation from the initial status.
Δq_j	Incremental actuation length of the j^{th} cable within each control time step, calculated from actuation kinematics.
Δq_{ja}	Incremental actuation length of the j^{th} cable for motor input within each control time step.

$$ {}^{bi}\mathbf{T}_{ui} = \begin{bmatrix} \mathbf{Rot}(\hat{\mathbf{x}}_{bi}, \alpha_i) & h\hat{\mathbf{z}}_{bi} \\ \mathbf{0} & 1 \end{bmatrix}, \quad {}^{ui}\mathbf{T}_{ei} = \begin{bmatrix} \mathbf{Rot}(\hat{\mathbf{y}}_{ei}, \beta_i) & h\hat{\mathbf{z}}_{ei} \\ \mathbf{0} & 1 \end{bmatrix} \tag{3} $$

where $Rot(\hat{n}, \theta)$ represents the rotation matrix about the axis $\hat{n}$ with an angle θ.

Next, the point $\mathbf{p}_{e,i,j}$ can be expressed in {bi} as follows.

$$ {}^{bi}\mathbf{p}_{e,i,j} = {}^{bi}\mathbf{T}_{ei}\,{}^{ei}\mathbf{p}_{e,i,j}. \tag{4} $$

The length of the j^{th} cable in the i^{th} universal joint is calculated by

$$ l_{i,j} = \| {}^{bi}\mathbf{p}_{e,i,j} - {}^{bi}\mathbf{p}_{b,i,j} \| . \tag{5} $$

Lastly, the actuation length required for the j^{th} cable to reach the target joint angles (α_i, β_i) can be expressed as follows.

$$ q_j = \sum_{i=1}^{n_j} \| \left({}^{bi}\mathbf{T}_{ei} - \mathbf{I}_{4\times4} \right) {}^{bi}\mathbf{p}_{b,i,j} \| - 2n_j h. \tag{6} $$

4.2. Closed-loop puller-follower controller

With the help of the two magnetic rotary sensors integrated in each universal joint providing joint angle feedback, a closed-loop puller-follower controller is proposed. Hence, the closed-loop joint angle control and the cable tension maintenance for all the sections are carried out simultaneously in the CDHM system with this controller.

As the three driving cables of each section are antagonistic, the tension on one cable might be affected by the other two cables for the same section. When the CDHM is in its initial state, all cables are first pre-tensioned to avoid slackness. The pre-tension process is described in Section 5.2.

The core design philosophy of the puller-follower controller is that the puller cables drive the universal joint to a desired pose, while the follower cables maintain the tensions on the cables to avoid slackness and fracture. Please note that one or two cables can be puller cables within the three cables for each universal joint, while the others are follower cables. The puller-follower controller was shown effective to reduce gradual cable slackness or over-tension in [23]. But the effectiveness was only tested in a single section. The efficacy of the proposed control scheme is further examined here, taking into consideration the coupling from all the proximal sections. e.g. For the j^{th} cable in the i^{th} section, coupling from the 1st section and the $(n_j-1)^{th}$ section is included.

The proposed puller-follower controller takes two sets of control inputs: the desired joint angles (α_{id}, β_{id}) and the desired cable elongation length $(\varepsilon_{jd}, \varepsilon'_{jd})$.

Firstly, a PD (proportional–derivative) controller is used for the joint angle control. The desired joint angles (α_{id}, β_{id}), as shown in the blue rectangle in Fig. 7, are compared with the actual joint angles (α_{ia}, β_{ia}) measured by the joint sensors. The resultant angle differences $(\tilde{\alpha}_i, \tilde{\beta}_i)$, as

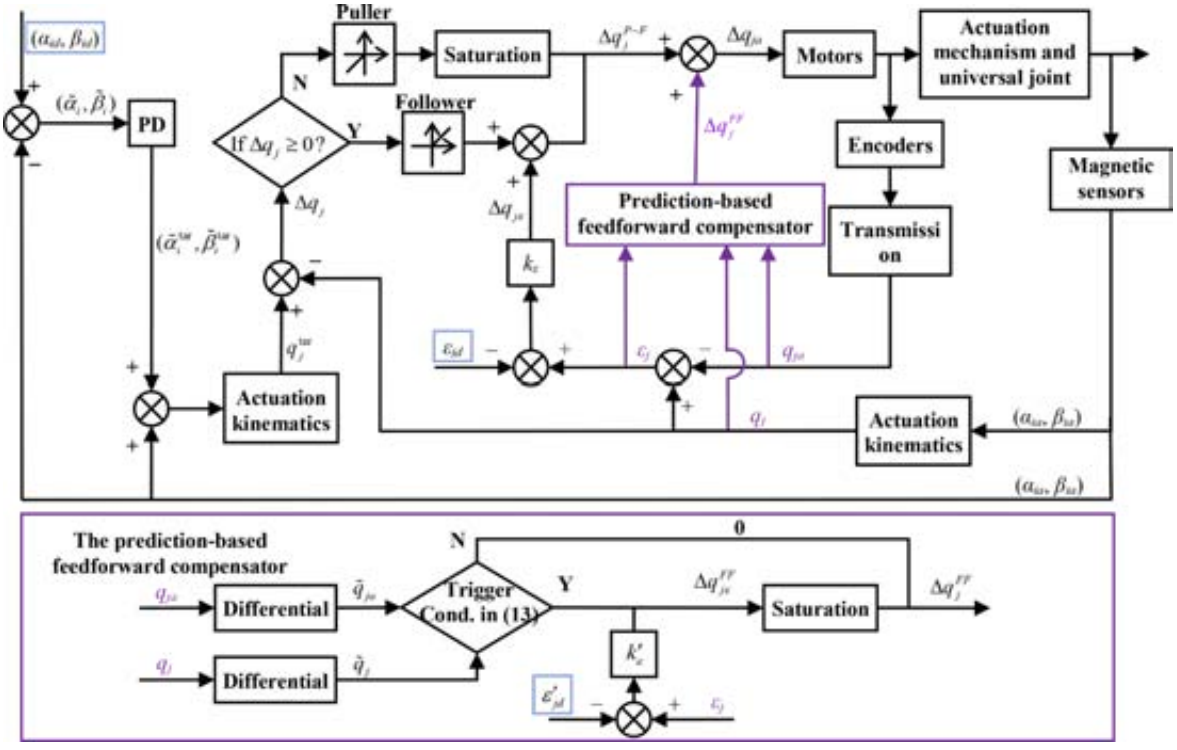

Fig. 7. Multi-section puller-follower closed-loop controller with a prediction-based feedforward compensator.

well as their variations compared to the last control time step $(\Delta\widetilde{\alpha}_i, \Delta\widetilde{\beta}_i)$, are inputs to the PD controller:

$$\begin{bmatrix} \widetilde{\alpha}_i^{\text{tar}} \\ \widetilde{\beta}_i^{\text{tar}} \end{bmatrix} = k_p \begin{bmatrix} \widetilde{\alpha}_i \\ \widetilde{\beta}_i \end{bmatrix} + k_d \begin{bmatrix} \Delta\widetilde{\alpha}_i \\ \Delta\widetilde{\beta}_i \end{bmatrix}, \tag{7}$$

where $(\widetilde{\alpha}_i^{\text{tar}}, \widetilde{\beta}_i^{\text{tar}})$ are the control output of the PD controller; k_p and k_d are the proportional and derivative gains.

Following the actuation kinematics model in Eqs. (1) to (6), the target actuation length q_j^{tar} and the current actuation length q_j are calculated from the target joint angles $(\widetilde{\alpha}_i^{\text{tar}} + \alpha_{ia}, \widetilde{\beta}_i^{\text{tar}} + \beta_{ia})$ and the sensed joint angles $(\alpha_{ia}, \beta_{ia})$, respectively.

Next, the target incremental actuation length for the driving cable is calculated as follows:

$$\Delta q_j = q_j^{\text{tar}} - q_j. \tag{8}$$

Also, the cable elongation ε_j is assumed to be the cable length difference calculated from the encoder reading and from the actuation kinematics:

$$\varepsilon_j = q_j - q_{ja}. \tag{9}$$

The puller-follower controller behaves differently according to the values of Δq_j and ε_j.

If $\Delta q_j \geq 0$, the cable will be released (i.e., as a follower cable). The possible slackness in this cable will be compensated according to the elongation ε_j. A proportional controller is hence employed to track the desired cable elongation length ε_{jd}, as shown in the blue rectangle in Fig. 7, in the follower cable:

$$\Delta q_{j\varepsilon} = k_\varepsilon(\varepsilon_j - \varepsilon_{jd}), \tag{10}$$

Where k_ε is a proportional gain.

The control output $\Delta q_{j\varepsilon}$ of the proportional controller is used for the elongation compensation. Hence, the output of the puller-follower controller is given by Eq. (11).

$$\Delta q_j^{P-F} = \Delta q_j + \Delta q_{j\varepsilon}, (\text{If} \Delta q_j \geq 0) \tag{11}$$

If $\Delta q_j < 0$, the cable will be pulled (i.e., as a puller cable). In this condition, the cable elongation, which can be calculated as in Eq. (9), will not be controlled unless it exceeds an upper limit $\varepsilon_{j\max}$. Here the output of the puller-follower controller is given by Eq. (12).

$$\Delta q_j^{P-F} = \begin{cases} k_\varepsilon(\varepsilon_j - \varepsilon_{j\max}), & \varepsilon_j \geq \varepsilon_{j\max} \\ \Delta q_j, & \varepsilon_j < \varepsilon_{j\max} \end{cases}, (\text{If} \Delta q_j < 0). \tag{12}$$

In order to relieve the responding delay of the angle joints while the corresponding cables' roles are switched between the puller and the follower, a prediction-based feedforward compensator is incorporated to adjust the cable tensions rapidly, as shown in the purple rectangle in Fig. 7. The inputs of this compensator are $\widetilde{q}_j, \widetilde{q}_{ja}$ and ε_j.

According to the experimental results, there are two main kinds of phenomena appearing during the role switch: (1) The joint angles do not change while the corresponding cables are keeping actuated; (2) The joint angles change in the opposite direction of the target joint angles. The reasons of the two phenomena are that the cable tension is too loose for the puller cable or too tight for the follower cable.

To predict whether the cable tension need be adjusted rapidly, a trigger condition is designed as follows.

$$\begin{cases} \widetilde{q}_j > k_{tg}\widetilde{q}_{ja} & \text{If } \Delta q_j < 0 \\ \widetilde{q}_j < k_{tg}\widetilde{q}_{ja} & \text{If } \Delta q_j \geq 0 \end{cases}, \tag{13}$$

Where $\widetilde{q}_j$ and $\widetilde{q}_{ja}$ are the differential values (e.g., increments) of q_j and q_{ja}, respectively; k_{tg} is a trigger coefficient that is less than 1; and $\Delta q_j = q_j^{\text{tar}} - q_j$ is the difference with respect to the target q_j.

If the trigger condition is satisfied (i.e. the actual actuation length of the cable doesn't reflect in the theoretical actuation length calculated from the actual joint angles), an extra proportional controller is used to rapidly adjust the cable tension with a desired cable elongation length ε'_{jd} and a proportional gain k'_ε:

$$\Delta q_{j\varepsilon}^{FF} = k'_\varepsilon(\varepsilon_j - \varepsilon'_{jd}) \tag{14}$$

while its output is limited as follows.

$$\begin{aligned} \Delta q_j^{FF} &= \begin{cases} 0, & \Delta q_{j\varepsilon}^{FF} > 0 \\ k_{sa}\Delta q_j, & \Delta q_{j\varepsilon}^{FF} < k_{sa}\Delta q_j, \text{ If } \Delta q_j < 0; \ \Delta q_j^{FF} \\ \Delta q_{j\varepsilon}^{FF}, & Else \end{cases} \\ &= \begin{cases} 0, & \Delta q_{j\varepsilon}^{FF} < 0 \\ k_{sa}\Delta q_j, & \Delta q_{j\varepsilon}^{FF} > k_{sa}\Delta q_j, \text{ If } \Delta q_j \geq 0 \\ \Delta q_{j\varepsilon}^{FF}, & Else \end{cases} \end{aligned} \tag{15}$$

Then, the incremental actuation length Δq_{ja} is calculated by Eq. (16).

$$\Delta q_{ja} = \Delta q_j^{P-F} + \Delta q_j^{FF} \tag{16}$$

Last, the incremental actuation length Δq_{ja} for all the cables are sent to the corresponding motors that are working in the position-servo mode. The joint angle errors can be stabilized after several control time steps with the proposed controller.

4.3. Manipulator kinematics

Combining Eq. (2), the homogenous transformation matrix from $\{b1\}$ to $\{tip\}$ can be formulated as in Eq. (17).

$${}^{b1}\mathbf{T}_{tip} = \begin{bmatrix} {}^{b1}\mathbf{R}_{tip} & {}^{b1}\mathbf{p}_{tip} \\ \mathbf{0} & 1 \end{bmatrix} = \prod_{i=1}^{12} \begin{bmatrix} {}^{bi}\mathbf{R}_{b(i+1)} & {}^{bi}\mathbf{p}_{b(i+1)} \\ \mathbf{0} & 1 \end{bmatrix}. \tag{17}$$

where ${}^{bi}\mathbf{R}_{b(i+1)} = \mathbf{Rot}(\hat{\mathbf{x}}_{bi}, \alpha_i)\mathbf{Rot}(\hat{\mathbf{y}}_{ei}, \beta_i)$ and ${}^{bi}p_{b(i+1)} = \begin{bmatrix} (l_{tube} + h)sin\beta_i \\ -(l_{tube} + h)sin\alpha_i cos\beta_i \\ h + (l_{tube} + h)cos\alpha_i cos\beta_i \end{bmatrix}$.

Similarly, the homogenous transformation matrix from $\{b1\}$ to $\{ui\}$ can be derived as

$${}^{b1}\mathbf{T}_{ui} = \begin{bmatrix} {}^{b1}R_{ui} & {}^{b1}\mathbf{p}_{ui} \\ \mathbf{0} & 1 \end{bmatrix} = \begin{cases} \prod_{k=1}^{i-1}({}^{bk}\mathbf{T}_{b(k+1)}) & \mathbf{T}_{ui}, i \geq 2 \\ {}^{b1}\mathbf{T}_{u1} & i = 1 \end{cases}. \tag{18}$$

As for the instantaneous kinematics, the linear Jacobian matrix for the i^{th} section is in Eq. (19).

$$\begin{aligned} \mathbf{J}_{iv} &= \begin{bmatrix} \frac{\partial^{bi}\mathbf{p}_{b(i+1)}}{\partial\alpha_i} & \frac{\partial^{bi}\mathbf{p}_{b(i+1)}}{\partial\beta_i} \end{bmatrix} \\ &= \begin{bmatrix} 0 & (l_{tube} + h)\cos\beta_i \\ -(l_{tube} + h)\cos\alpha_i\cos\beta_i & (l_{tube} + h)\sin\alpha_i\sin\beta_i \\ -(l_{tube} + h)\sin\alpha_i\cos\beta_i & -(l_{tube} + h)\cos\alpha_i\sin\beta_i \end{bmatrix}. \end{aligned} \tag{19}$$

The angular velocity Jacobian for the i^{th} section is derived as follows.

$$\mathbf{J}_{i\omega} = \begin{bmatrix} 1 & 0 \\ 0 & \cos\alpha_i \\ 0 & \sin\alpha_i \end{bmatrix}. \tag{20}$$

The Jacobian for the 12-section manipulator can be written in Eq. (21).

$$\mathbf{J}_i = \begin{bmatrix} \mathbf{T}_1 & {}^{b1}\mathbf{R}_{b2}\mathbf{T}_2 & \cdots & {}^{b1}\mathbf{R}_{bi}\mathbf{T}_i & \cdots & {}^{b1}\mathbf{R}_{b12}\mathbf{T}_{12} \\ \mathbf{J}_{1\omega} & {}^{b1}\mathbf{R}_{b2}\mathbf{J}_{2\omega} & \cdots & {}^{b1}\mathbf{R}_{bi}\mathbf{J}_{i\omega} & \cdots & {}^{b1}\mathbf{R}_{b12}\mathbf{J}_{12\omega} \end{bmatrix} \tag{21}$$

where $\mathbf{T}_1 = \mathbf{J}_{1v} - ({}^{b1}\mathbf{p}_{tip} - {}^{b1}p_{b2})^\wedge\mathbf{J}_{1\omega}$, $\mathbf{T}_2 = \mathbf{J}_{2v} - ({}^{b1}\mathbf{p}_{tip} - {}^{b1}p_{b3})^\wedge\mathbf{J}_{2\omega}$, $\cdots$, $\mathbf{T}_i = \mathbf{J}_{iv} - ({}^{b1}\mathbf{p}_{tip} - {}^{b1}p_{b(i+1)})^\wedge\mathbf{J}_{i\omega}$, $\cdots$, and $\mathbf{T}_{12} = \mathbf{J}_{12v}$.

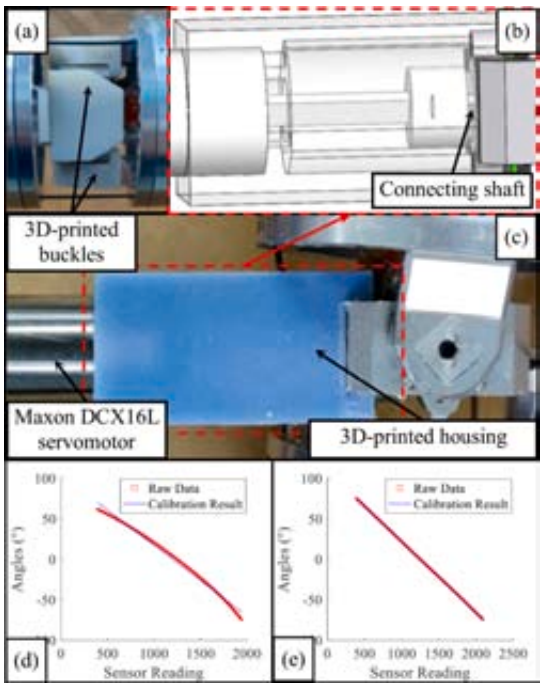

Fig. 8. Sensor calibration: (a) the zero-position calibration setup, (b, c) input-output calibration setup for the magnetic sensor, (d and e) calibration results without and with the shielding cases.

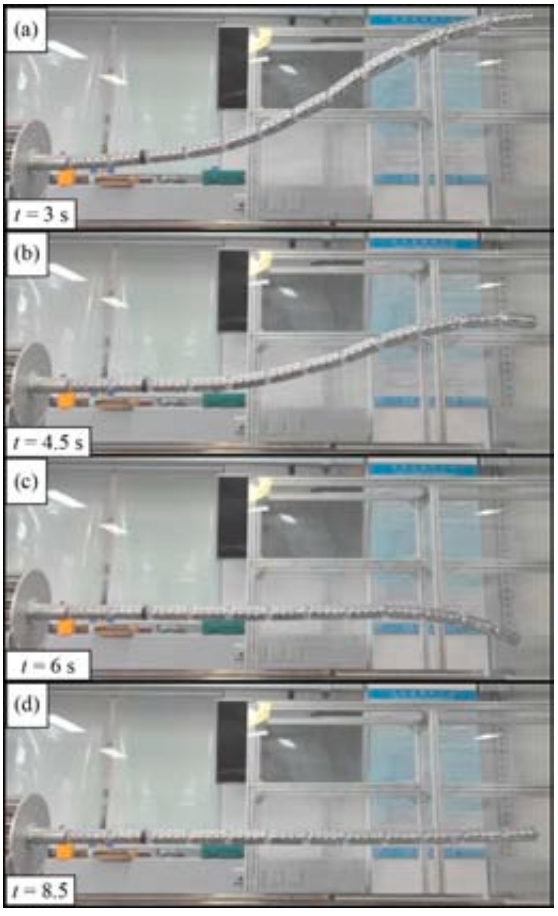

Fig. 9. The automatic straightening procedure: (a) automatic pre-tension done; (b, c) automatic straightening; (d) automatic straightening done.

The Jacobians can be utilized to solve inverse kinematics problems to accomplish tip target-reaching tasks, while satisfying additional constraints (e.g., obstacle avoidance or follow-the-tip planning) utilizing redundancy resolution [30].

5. Experimental characterization

Various experiments have been carried out to characterize the CDHM's performance. Before the conducted experiments, the magnetic rotary sensors were calibrated to verify the sensing precision. The CDHM system then underwent an automatic straightening procedure to initiate a straight and pre-tensioned state. Next, the performance of the CDHM system was demonstrated through a follow-the-tip motion experiment and payload capability tests.

5.1. Calibration of the magnetic sensor

With respect to each rotary magnet disk, the AS5600 magnetic potentiometers shall be calibrated to obtain the actual input-output relations. The zero positions of the sensors corresponding to a straight manipulator configuration were first obtained. For each section, the universal joint was set to an initial state (i.e., $\alpha_i = \beta_i = 0$) by four 3D-printed fixtures, as shown in Fig. 8(a). The corresponding readings from the two sensors were recorded as the zero references.

To verify the accuracy, the sensor input-output curve was calibrated within the joint angle range which is $\pm 45^\circ$ During the process, a Maxon DCX16L servomotor, with GPX-16 gearhead and ENX16 encoder, was connected to the connecting shaft of the universal joint via a 3D- printed housing to provide the actual angle of sensor, as shown in Fig. 8(b-c).

When the AS5600 magnetic potentiometers were not covered with the silicone steel shielding cases, the calibration result of a certain sensor is shown in Fig. 8(d). The resultant sensor input-output curve was not linear, RMSE $= 4.104^\circ$ for the linear regression, mainly due to the magnetic interference between the two neighborly placed magnetic disks integrated in one universal joint. To diminish the interference, silicon steel shielding cases were mounted. Improved results, RMSE $= 0.2022^\circ$, were obtained when the shielding case was added, as shown in Fig. 8(e).

After adding shielding cases, all the 24 magnetic potentiometers were calibrated for both the zero references and the input-output curves before usage.

5.2. Automatic straightening and pre-tension

In order to make the CDHM always start with a straight and pre-tensioned initial state, an automatic straightening procedure is desired. The procedure includes two steps: the automatic pretension step and the automatic straightening step.

Before the two steps, the motor current was first experimentally obtained for an appropriate pre-tension on the cable. A dynamometer was attached to one end of the cable, and the driving motor was set to work in the current mode to tension the cable. Then the motor current was adjusted such that the corresponding cable tension was maintained at about 100 N. The motor current values were recorded as the pre-tension current references for the automatic pre-tension step.

In the automatic pre-tension step, all the EPOS 36/2 motor controllers are set to work in the position mode and then loosen the cables for a short distance (e.g., 20 mm in the following experiments). Then, the motor controllers are switched to the current mode to tension the cables until the corresponding pre-tension motor current is sustained for several seconds (e.g., 3 s in the following experiments).

During the automatic straightening step, the linearly descending target joint angles (i.e., the target angles are set to zero gradually) for the proximal four sections (the 1st to 4th sections) are sent to the proposed puller-follower controller in the period time from 3 s to 4.5 s. Then the target joint angles for the next four sections and the last four sections are

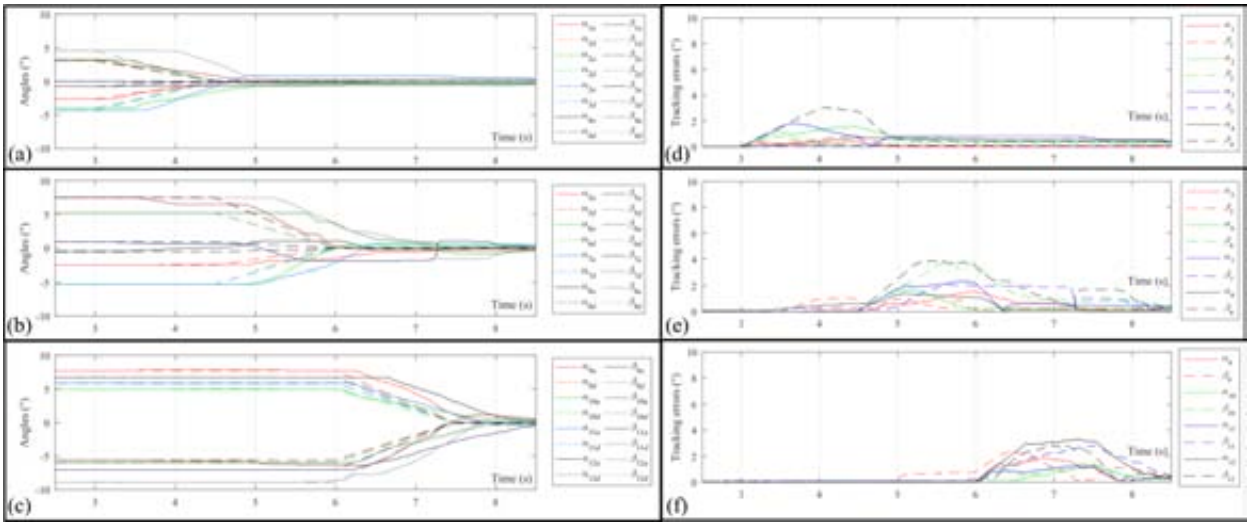

Fig. 10. Joint angles during the automatic straightening for (a) the 1st−4th sections, (b) the 5th−8th sections, and (c) the 9th−12th sections and the tracking errors for (d) the 1st−4th sections, (e) the 5th−8th sections, and (f) the 9th−12th sections.

successively set to zero gradually for the same duration of 1.5 s. This procedure continues until all joint angles of the 12 sections are stabilized around zero within the ±0.5° tolerance with acceptable tensions in all the cables.

To validate the effectiveness of the automatic straightening procedure, the CDHM was set to a random initial state (all 24 joint angles were not 0°). The automatic straightening was then carried out, and the procedure is shown in Fig. 9. Please refer to the multimedia extension for the process of the experiment. The CDHM completed the automatic pretension within 3 s and automatic straightening within the next 5.5 s (at 8.5 s in Fig. 10).

The target values, the actual values and the tracking errors of the joint angles were recorded and plotted in Fig. 10. It can be seen that some of the joint angle responded relatively slow (e.g., β_{4a} during 3−4 s, β_{8a} during 4.5−5.2 s). This may be due to i) the movement of the proximal universal joints, ii) dry friction at the contacts along the actuation cable for the stick-slip like vibration, and iii) the mild parameter setting in the puller-follower PD controller, since an aggressive parameter setting easily causes the CDHM to fluctuate even longer than the present settle time.

5.3. Follow-the-tip path tracking experiment

A follow-the-tip path tracking was conducted to demonstrate the kinematic redundancy of the CDHM system. Several works have proposed various approaches to realize the follow-the-tip path tracking for redundant manipulators, such as the sequential quadratic programming optimization approach [5] and the prediction lookup & interpolation algorithm in [22]. This work adopts a concise follow-the-tip motion tracking algorithm similar to the one proposed in [31] for analytically parameterized continuous paths. The approach is described as follows.

Firstly, the path ${}^{w}\boldsymbol{p}_{path}(s) = [x_{\text{path}}(s)\ y_{\text{path}}(s)\ z_{\text{path}}(s)]^T$ is parametrized by $s \in [0,1]$. It is then considered that the mobile base can adjust the starting pose of the snake-like manipulator such that the manipulator's tip is initially (i.e., at the straight state) on the starting position of the target path aligned with the direction of the curve tangent. Next, the snake-like manipulator is actuated by the feeding motor to follow the path for each control time step with an arbitrary feeding length d.

Experiments were conducted to verify the effectiveness of the proposed controller and the follow-the-tip path tracking algorithm. A 3D path comprising 3 consecutively tangent arcs, each with a 300 mm radius of curvature, was generated. The CDHM system was controlled to perform the follow-the-tip motion while tracking the path. The video

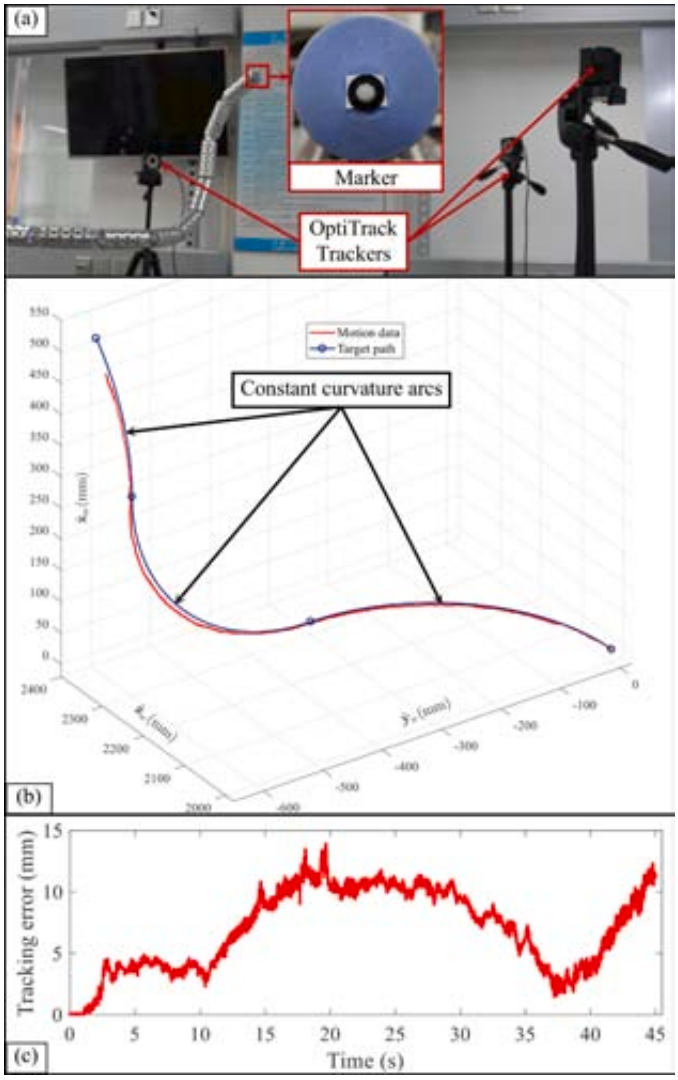

Fig. 11. Follow-the-tip path tracking experiment: (a) experimental setup, (b) actual tip positions compared to the target path, (c) the tracking errors.

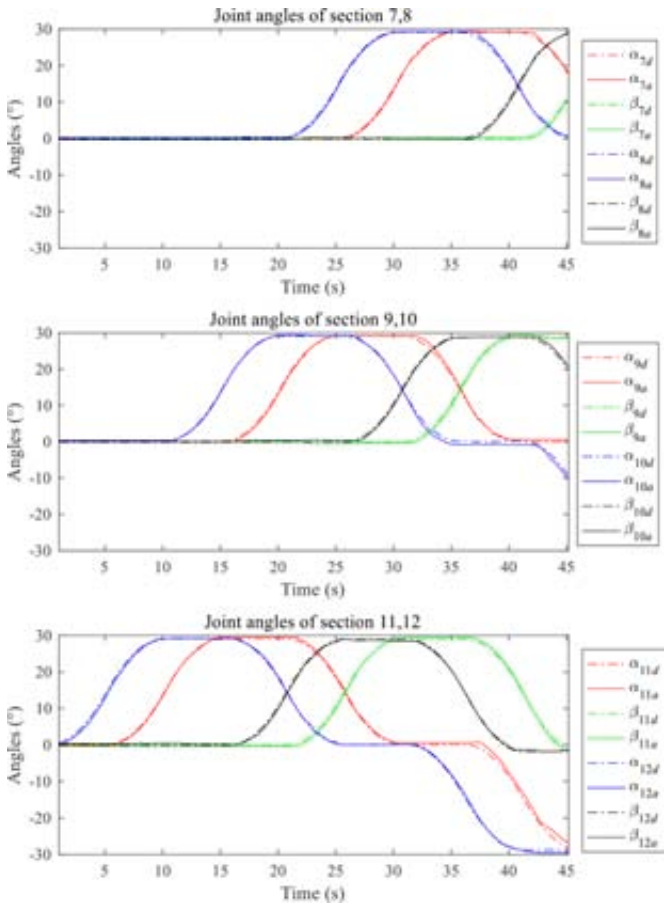

Fig. 12. The joint angles of the follow-the-tip motion.

clip for this procedure is available in the multimedia extension.

To evaluate the tracking performance, an optical motion capture system OptiTrack (NaturalPoint, Inc.) was used to obtain the tip position of the CDHM. Six trackers were set around the CDHM system to track the marker attached to the tip section, as shown in Fig. 11(a). The comparison between the motion data and the target path is shown in Fig. 11 (b). The minimum distances between the measured positions and the positions on the target path were then regarded as the tracking error, as shown in Fig. 11(c). The average tracking error was 6.94 mm, about 0.385% of the CDHM total length, whereas maximum tracking error was 13.91 mm.

The target joint angles and the corresponding actual joint angles obtained from the sensors for the distal 6 sections (i.e. the 7th to 12th sections) were recorded and are plotted in Fig. 12. With the proposed controller, the actual angles were able to track the target angles with the average angle tracking error of 0.283° over all joints and the maximum angle error was 1.906° The mean and maximum absolute elongation errors (i.e. the difference between ε_{jd} and ε_j) were 0.356 mm and 2.744 mm, respectively. The elongation errors around 0 mm would indicate that desired tensions in these cables are maintained.

5.4. Payload capability tests

Due to the manipulator's long reach, a distal payload can substantially affect the pose accuracy of the manipulator, as shown in Fig. 13(a). The proposed controller can improve such adverse effects by reducing the joint angle errors. Experiments were hence carried out to demonstrate the improved payload capability using the proposed puller-follower controller. The CDHM was set at its straight state, and a 200-g payload and a 500-g payload were then separately applied to the distal end of the CDHM. Using the same optical tracking system as shown in Fig. 11(a), the tip positions of the CDHM in both the unloaded and the loaded conditions were obtained. The experiment was repeated for three times and the results are presented in Fig. 13(b). With the proposed controller, the position errors were controlled under 15 mm for all payload conditions. Similarly, the 0.5° actuation dead zone might have contributed to these errors.

In order to further demonstrate the performance of the proposed controller against external loads, a follow-the-tip path tracking experiment was performed, with 0, 200 g, and 500 g payload added on the distal end, as demonstrated in Fig. 14 and the multimedia extension. The procedure showed the CDHM's capability to track target paths with external tip disturbances.

5.5. Application demonstration

To demonstrate the operational capability of the proposed CDHM system, a center wing tank model of a commercial airplane was established with aluminum profiles and acrylic board. Then the CDHM system was used to inspect several cavities of the model with a 200-g payload for the simulation of functional end-effectors, as shown in Fig. 15.

6. Conclusion

This paper proposes a 12-section CDHM system with 24 DoFs and a closed-loop controller for enhanced motion precision and payload capability. The mechanical design of the CDHM is described and the kinematics model is developed. A puller-follower controller is proposed to achieve tension maintenance and closed-loop joint angle control based on the magnetic potentiometer sensor feedback.

Several experiments were carried out to validate the performance of the CDHM and its controller. Via proper sensor calibration and initialization of a pretension procedure, the CDHM could accomplish follow-the-tip path tracking motion with an average tracking error of 6.94 mm. Owing to the proposed controller, the joint angles followed the target angles at an acceptable precision (with 0.283° average error) and the cable tensions were maintained to track the target elongation value (with a 0.356 mm average error).

Future works mainly concern two aspects. Firstly, the teleoperation of the CDHM system, especially with redundancy resolution, shall be conducted for industrial operations in confined spaces, to fully exploit

Fig. 13. Payload capability test: (a) the straight manipulator deflected by a 500-g weight without the closed-loop controller; (b) tip position errors under different payload conditions.

Fig. 14. Path tracking motions with 500-g, 200-g payloads and without payload.

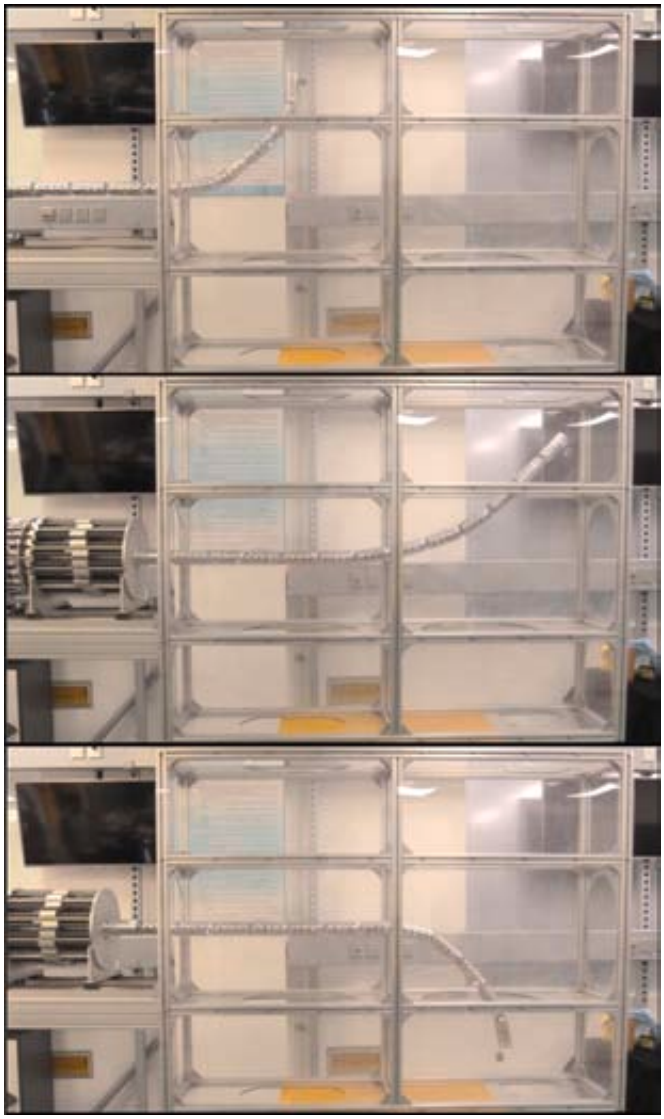

Fig. 15. Inspections to different cavities of a center wing tank model.

the system's motion capability. Secondly, visual servoing for further improvement of the tip positioning accuracy can be investigated in order to alleviate the effects brought by the 0.5° actuation dead zone in the joints.

CRediT authorship contribution statement

Yang Zheng: Conceptualization, Methodology, Software, Validation, Data curation, Writing – original draft, Writing – review & editing, Visualization. **Baibo Wu:** Conceptualization, Methodology, Software, Validation, Data curation, Writing – review & editing. **Yuyang Chen:** Writing – original draft, Writing – review & editing. **Lingyun Zeng:** Methodology, Software, Validation. **Guoying Gu:** Resources, Supervision, Project administration, Funding acquisition. **Xiangyang Zhu:** Resources, Supervision, Project administration, Funding acquisition. **Kai Xu:** Conceptualization, Methodology, Resources, Writing – review & editing, Supervision, Project administration, Funding acquisition.

Declaration of Competing Interest

The authors declare that they have no known competing financial interests or personal relationships that could have appeared to influence the work reported in this paper.

Acknowledgement

This work was supported in part by the National Key R&D Program of China (Grant Nos. 2019YFB1311204 and 2017YFC0110800), and in part by the National Natural Science Foundation of China (Grant Nos. 51722507 and 51435010).

Supplementary materials

Supplementary material associated with this article can be found, in the online version, at doi:10.1016/j.mechatronics.2021.102605.

Reference

[1] Westkämper E, Schraft RD, Schweizer M, Herkommer TF, Meißner A. Task-oriented programming of large redundant robot motion. Robot Comput Integr Manuf 1998; 14:363–75.
[2] Buckingham R, Graham A. Nuclear snake-arm robots. Ind Rob 2012;39:6–11.
[3] Kim Y-J, Cheng S, Kim S, Iagnemma K. A stiffness-adjustable hyperredundant manipulator using a variable neutral-line mechanism for minimally invasive surgery. IEEE Trans. Robot 2014;30:382–95.
[4] Xidias EK. Time-optimal trajectory planning for hyper-redundant manipulators in 3D workspaces. Robot Comput Integr Manuf 2018;50:286–98.
[5] Palmer D, Cobos-Guzman S, Axinte D. Real-time method for tip following navigation of continuum snake arm robots. Rob Auton Syst 2014;62:1478–85.
[6] V.C. Anderson, R.C. Horn, Tensor arm manipulator, in: U.S.P. Office, United States, 1970.
[7] Chirikjian GS, Burdick JW. Design and experiments with a 30 DOF robot. IEEE international conference on robotics and automation (ICRA). IEEE; 1993. p. 113–9.
[8] E. Paljug, T. Ohm, S. Hayati, The JPL serpentine robot: a 12 DOF system for inspection, IEEE international conference on robotics and automation (ICRA), Washington, DC, 1995, pp. 3143–8.
[9] Wolf A, Brown HB, Casciola R, Costa A, Schwerin M, Shamas E, Choset H. A mobile hyper redundant mechanism for search and rescue tasks. IEEE/RSJ international conference on intelligent robots and systems (IROS). 2003. p. 2889–95.
[10] H.B. Brown, M. Schwerin, E. Shammas, H. Choset, Design and control of a second-generation hyper-redundant mechanism, IEEE/RSJ international conference on intelligent robots and systems (IROS), San Diego, CA, USA, 2007, pp. 2603–8.
[11] S. Tappe, J. Pohlmann, J. Kotlarski, T. Ortmaier, Towards a follow-the-leader control for a binary actuated hyper-redundant manipulator, IEEE/RSJ international conference on intelligent robots and systems (IROS), Hamburg, Germany, 2015, pp. 3195–210.
[12] S. Hirose, S. Ma, Coupled tendon-driven multijoint manipulator, IEEE international conference on robotics and automation (ICRA), Sacramento, CA, USA, 1991, pp. 1268–75.
[13] T. Ota, A. Degani, D. Schwartzman, B. Zubiate, J. McGarvey, H. Choset, M.A. Zenati, A novel highly articulated robotic surgical system for epicardial ablation, Annual international conference of the IEEE engineering in medicine and biology society (EMBS), Vancouver, Canada, 2008, pp. 250–3.

[14] Tang L, Wang J, Zheng Y, Gu G, Zhu L, Zhu X. Design of a cable-driven hyper-redundant robot with experimental validation. Int. J. Adv. Robot. Syst 2017;14.
[15] Xu W, Liu T, Li Y. Kinematics, dynamics, and control of a cable-driven hyper-redundant manipulator. IEEE ASME Trans Mechatron 2018;23:1693–704.
[16] Endo G, Horigome A, Takata A. Super dragon: a 10-m-long-coupled tendon-driven articulated manipulator. IEEE Robot. Autom. Lett 2019;4:934–41.
[17] Tang J, Zhang Y, Huang F, Li J, Chen Z, Song W, Zhu S, Gu J. Design and kinematic control of the cable-driven hyper-redundant manipulator for potential underwater applications. Appl Sci 2019;9:1142.
[18] Walker ID. Continuous backbone "continuum" robot manipulators. ISRN Robot. 2013;2013:1–19.
[19] W. McMahan, V. Chitrakaran, M. Csencsits, D.M. Dawson, I.D. Walker, B.A. Jones, M. Pritts, D. Dienno, M. Grissom, C.D. Rahn, Field trials and testing of the OctArm continuum manipulator, IEEE international conference on advanced robotics (ICAR), Orlando, FL, USA, 2006, pp. 2336–41.
[20] Liu S, Yang Z, Zhu Z, Han L, Zhu X, Xu K. Development of a dexterous continuum manipulator for exploration and inspection in confined spaces. Ind Rob : 2016;43:284–95.
[21] Burgner-Kahrs J, Rucker DC, Choset H. Continuum robots for medical applications: a survey. IEEE Trans. Robot 2015;31:1261–80.
[22] Tang L, Zhu L, Zhu X, Gu G. Confined spaces path following for cable-driven snake robots with prediction lookup and interpolation algorithms. Sci. China Technol. Sci 2019;63:255–64.
[23] B. Wu, L. Zeng, Y. Zheng, S.a. Zhang, X. Zhu, K. Xu, A closed-loop controller for cable-driven hyper-redundant manipulator with joint angle sensors, IEEE international conference on robotics and biomimetics (ROBIO), Dali, Yunnan, China, 2019, pp. 2433–8.
[24] Buckingham RO, Graham AC. Robotic arms. US: Oliver Crispin Robotics Limited; 2012.
[25] Graham AC, Buckingham RO. Robotic arm. US: Oliver Crispin Robotics Limited; 2014.
[26] Potkonjak V, Svetozarevic B, Jovanovic K, Holland O. The puller-follower control of compliant and noncompliant antagonistic tendon drives in robotic. Int. J. Adv. Robot. Syst 2011;8:143–55.
[27] U. Jeong, H. In, H. Lee, B.B. Kang, K.-J. Cho, Investigation on the control strategy of soft wearable robotic hand with slack enabling tendon actuator, IEEE international conference on robotics and automation (ICRA), Seattle, Washington, 2015, pp. 5004–5009.
[28] Kawaharazuka K, Kawamura M, Makino S, Asano Y, Okada K, Inaba M. Antagonist inhibition control in redundant tendon-driven structures based on human reciprocal innervation for wide range limb motion of musculoskeletal humanoids. IEEE Robot. Autom. Lett 2017;2:2119–26.
[29] X. Cui, W. Chen, G. Yang, Y. Jin, Closed-loop control for a cable-driven parallel manipulator with joint angle feedback, IEEE international conference on advanced intelligent mechatronics (AIM), Wollongong, Australia, 2013, pp. 625–30.
[30] Chiaverini S. Singularity-robust task-priority redundancy resolution for real-time kinematic control of robot manipulators. IEEE Trans Robot Autom 1997;13:398–410.
[31] Choset H, Henning W. A follow-the-leader approach to serpentine robot motion planning. J Aerosp Eng 1999;12:65–73.

Yang Zheng received a B.S. degree from the College of Mechanical and Electrical Engineering, Hohai University, Nanjing, China, in 2015. He is currently pursuing his Ph.D. degree in the School of Mechanical engineering, Shanghai Jiao Tong University, Shanghai, China. His-research interests include Cable-driven mechanisms and redundant manipulators.

Baibo Wu received a B.S. degree from the School of Mechatronics Engineering, Harbin Institute of Technology, Harbin, China, in 2016. He received an M.S. degree from the School of Astronautics, Harbin Institute of Technology, Harbin, China, in 2018. He is pursuing his Ph.D. degree in the School of Mechanical Engineering, Shanghai Jiao Tong University, Shanghai, China. His-research interests include surgical robots, bio-mechatronics and continuum mechanisms.

Yuyang Chen received a B.S. degree from the School of Mechanical Engineering, Zhejiang University, Hangzhou, China, in 2015. He is currently pursuing his Ph.D. degree in the University of Michigan–Shanghai Jiao Tong University Joint Institute, Shanghai Jiao Tong University, Shanghai, China. His-research interests include surgical robots and continuum mechanisms.

Lingyun Zeng received the B.S. degree from the Wuhan University, Wuhan, China, in 2017 and the M.S. degree in Mechanical Engineering from Shanghai Jiao Tong University, Shanghai, China, in 2020. His-research interests include medical robotics, continuum robotics, and mechanics-based modeling and control.

Guoying Gu received the B.E. degree (with honors) in electronic science and technology, and the Ph.D. degree (with honors) in mechatronic engineering from the Shanghai Jiao Tong University, Shanghai, China, in 2006 and 2012, respectively. Since October 2012, he was at the Shanghai Jiao Tong University, where he is currently appointed as a Professor of School of Mechanical Engineering. He was a Humboldt Postdoc Fellow with the University of Oldenburg, Germany. His-research interests include soft robotics, smart materials actuated systems, bio-inspired robot design, and motion control.

Xiangyang Zhu received the B.S. degree from the Department of Automatic Control Engineering, Nanjing Institute of Technology, Nanjing, China, in 1985, the M.Phil. degree in instrumentation engineering and the Ph.D. degree in automatic control engineering, both from the Southeast University, Nanjing, China, in 1989 and 1992, respectively. Since June 2002, he has been with the School of Mechanical Engineering, Shanghai Jiao Tong University, Shanghai, China, where he is currently a Changjiang Chair Professor and the Director of the Robotics Institute. His-current research interests include robotic manipulation planning, human–machine interfacing, and biomechatronics.

Kai Xu received a B.E. and an M.S. from the Department of Precision Instruments and Mechanology, Tsinghua University, Beijing, China, in 2001 and 2004, respectively, and a Ph.D. (with distinction) from the Department of Mechanical Engineering, Columbia University, New York, NY, in 2009. He is now a Professor with the School of Mechanical Engineering, Shanghai Jiao Tong University, Shanghai, China, and the Director of the Robotics Innovation and Intervention Laboratory. His-research interests include surgical robots, prosthetic hands, flexible manipulators, special industrial robots, and continuum mechanisms.